X-ray Study of the Paracrystalline Nature of Crystallized 70*S* Ribosome Lamellae

By E. D. Kuckuk

Physiologisches Institut der Universität Göttingen, Humboldtallee 7, Göttingen, Federal Republic of Germany

and R. Hosemann

Gruppe Parakristallforschung, c/o Bundesanstalt für Materialprüfung (BAM), Berlin 45, Unter den Eichen 44–46, Federal Republic of Germany

Abstract

If a mixed organic solvent is added to a ribosome solution and stored at 277 K in a crystallization chamber, thin lamellae of a few μm diameter can be obtained. Under the electron microscope, tetragonal face-centred macrocells of $b = 40$ and $c = 55$ nm are visible. These findings are substantiated by X-ray small- and wide-angle diffraction which leads to macrocells of $b = 42$ and $c = 52$ nm and establishes the third dimension of the macrocell with $a = 42$ nm. Mainly $0kl$ reflections appear. From their line widths, it follows that each lamella consists of at least $15 \times 15 \times 15$ macrocells with small paracrystalline distortions $g_s \simeq 1 \cdot 5\%$, whilst their $6 \times 8 \times 12$ subcells with $a_0 = 7 \cdot 1$, $b_0 = 5 \cdot 3$ and $c_0 = 4 \cdot 3$ nm have large fibrillary distortions in the bc plane, similar to the aggregation of microparacrystals in stretched and annealed polymers. With a new method, the folding root of the Q function projected on the b axis can be analysed. Two compounds are placed in each macrocell, each consisting of about 136 cylinders of about 2·0 nm diameter and 7 nm length. They are aligned to fibrils of different lengths orthogonal to the bc plane and occupy about 47% of the macrocell. The residual volume is filled up with an 'amorphous phase' as in semicrystalline polymers. A comprehensive study of the existing literature leads to the conclusion that the 'crystalline phase' consists of two 70*S* ribosome tetramers and that the cylinders are obviously parts of two-stranded helices, whilst most of the RNA proteins are in the 'amorphous phase'. The biological significance of the ribosome crystals and the paracrystalline sublattice is described in detail in the *Discussion*.

I. Introduction

More and more papers have recently taken cognizance of the paracrystalline character of biogenetic matter. An outstanding example is native collagen from rat tail (Nemetschek & Hosemann, 1973*a*,*b*; Hosemann &

Nemetschek, 1973; Hosemann, Bonart & Nemetschek, 1974; Hosemann, Dreissig & Nemetschek, 1974; Hosemann, Weick, Vogel & Müller, 1974; Dreissig, Hosemann & Nemetschek, 1974) and the understanding of its calcification (Newesely, Hosemann & Uther, 1980). Wheeler & Lewis (1977) stated, for instance, 'The paracrystalline state may be regarded as one which is intermediate between amorphous and crystalline and will have properties between those of these two states. Having more disordered atomic arrangements than exist in the crystalline state, paracrystalline materials are more reactive, so that with a structure of this type bone apatite will more readily be able to fulfil its biological role of calcium ion control . . .'.

In the last 20 years, there has been enormous progress in our knowledge of the composition and interaction of ribosomal components. But until now very little has been known about their physical structure. Various X-ray scattering experiments have been made of ribosomes of different types of cells with dilute solutions or with concentrated gels by Zubay & Wilkins (1960), Klug, Holmes & Finch (1961), Langridge & Holmes (1962), Hill, Thompson & Anderegg (1969) and Venable, Spencer & Ward (1970). Small-angle X-ray studies have also been carried out on isolated ribosomal RNA by Rich & Watson (1954), Fuller (1961), Brown & Zubay (1960), Timasheff, Witz and Luzzati (1961), Spencer, Pigram & Littlechild (1969), Dibble (1964), Connors & Beeman (1972), Hill & Fessenden (1974) and Folkhard, Pilz, Kratky, Garrett & Stöffler (1975).

Moreover, a large number of electron-microscopical investigations have been conducted on the structure of ribosomes (Hall & Slayter, 1959; Huxley & Zubay, 1960; Hart, 1962, 1965; Spirin, Kiselev, Shakulov & Bogdanov, 1963; Nanninga, 1967, 1968; Bruskov & Kiselev, 1968; Lubin, 1968; Nonomura, Blobel & Sabatini, 1971; Tischendorf, Zeichhardt & Stöffler, 1975). Further details concerning the distribution of protein and RNA in ribosomal subunits has been provided by the neutron scattering studies of Moore,

Engelman & Schoenborn (1974, 1975). They found a radius of gyration for the $30S$ subunit of $7 \cdot 14$ nm and for the $70S$ a value of $7 \cdot 8$ nm, and hence a diameter of 18 and 20 nm respectively. Similar values have been established with neutron scattering by Parfait, Koch, Crichton, Haas & Stuhrmann (1978) ($6 \cdot 85$ and $7 \cdot 8$ nm for the $30S$ and $50S$, respectively).

X-ray small-angle scattering studies of concentrated gels revealed a wide range of spacings from $0 \cdot 33$ to 30 nm (Klug et al., 1961). Hill et al. (1969) describe the $70S$ ribosome as a slightly asymmetric particle having dimensions 16 × 18 × 20 nm, as elucidated by X-ray scattering from diluted ribosome solutions.

The hydrated ribosome has a series of characteristic X-ray scattering spacings which are identical with those found in diagrams of isolated rRNA (Zubay & Wilkins, 1960; Klug et al., 1961). Spencer et al. (1969) demonstrated by X-ray diffraction studies of crystalline specimens of fragments of rRNA that the crystallizable fragments contain regular two-stranded helices with a diffraction pattern like the A form of DNA. All these findings have been substantiated by chemophysical studies (Schlessinger, 1960; Bush & Sheraga, 1967), supporting the concept that about 70% of the rRNA in the ribosome has its bases stacked together and possesses many regions in which the single chain forms two-stranded helices by folding back upon itself. Langridge (1969; Langridge & Holmes, 1962) described a strong reflection from X-ray scattering experiments with concentrated ribosome gels as 'due to some periodicity in the ribosome'. On the basis of electron micrographs, Spirin et al. (1963), Hart (1965) and Bruskov & Kiselev (1968) describe some periodical features of $30S$ and $50S$ ribosomes. Recently published three-dimensional models of protein arrangements in the $30S$ subparticle, computed with protein near-neighbour information (Gaffney & Craven, 1978), also reveal some common features with ribosomal subcells and spacings similar to those reported in the present paper.

Electron micrographs do not afford sufficient resolution to provide any further information on the fine structure of the ribosome. This may be due to the disorder in the structure caused by dehydration during preparation and the irradiation with electrons. The hydration of the native ribosome is much higher than that of proteins or small spherical viruses (Lauffer & Bendet, 1954). This is also substantiated by the fact that X-ray diffraction patterns of ribosomes are strongly dependent on moisture content. In the dry state, a disordered diffraction pattern predominates which is largely attributed to the ribosomal proteins (Wilkins, Zubay & Wilson, 1959; Zubay & Wilkens, 1960; Klug, Holmes & Finch, 1961). The average of the dimensions measured by electron microscopy is about 20% smaller than that measured by X-ray diffraction.

Over the last 15 years, data from electron-microscopical investigations and chemical experiments have formed the basis for a series of models of the ribosomal structure (Bruskov & Kiselev, 1968; Cox, 1969; Hart, 1965; Lubin, 1968; Nonomura et al., 1971; Spirin et al., 1963; Tischendorf et al., 1975).

It is the aim of this paper to introduce the concept of paracrystallinity into the X-ray diffraction analysis of ribosomes. This modern analysis of X-ray diffraction has the big advantage of nondestructive testing of materials, which does not destroy the native state of biological systems and gives direct insight into their molecular structures, which are never crystalline. A comparison with electron micrographs based on this knowledge will confirm the obtained results. There is not space enough to explain the theory of paracrystals here in more detail. The six Appendices give some detailed explanations.* The reader may refer to the above mentioned papers on collagen and apatite and to the book by Hosemann & Bagchi (1962).

II. Preparation of the sample and recording of the micrographs

Escherichia coli cells were grown in a rich medium according to Deusser (1972) and harvested in their stationary phase. Isolation of $70S$ ribosomes was performed according to Weber (1972) with the exception that a buffer containing $0 \cdot 01$ mol dm^{-3} tris buffer/HCl, pH $7 \cdot 8$, $0 \cdot 02$ mol dm^{-3} $MgCl_2$, $0 \cdot 1$ mol dm^{-3} KCl, and 6×10^{-3} mol dm^{-3} 2-mercaptoethanol was used. The $70S$ ribosomes were subjected to further purification by applying them to a linear sucrose gradient (Paradies, Kuckuk, Klotz, Zerban & Deusser, 1974).

The micrograph shown in Fig. 1 was obtained simply by removing a complete crystal from the mother liquor, staining in $0 \cdot 5\%$ uranyl acetate without any further preparation, and observing under the electron microscope. Previous fixation in glutaraldehyde reduced the stability of the crystalline structure such that the latter eventually disintegrated, at the latest during irradiation with electrons. The X-ray diffraction patterns were obtained from about 30 to 40 crystallites which had been removed from the crystallization chamber by means of a glass capillary and exposed for 3–10 d at 277 K in an evacuated point-focusing Franks camera. The measurements were performed using nickel-filtered Cu $K\alpha$ radiation and a water-cooled rotating anode, GX-13, Elliot–Marconi, UK. In addition, X-ray small-angle scattering of a suspension of highly concentrated

---

* The six Appendices have been deposited with the British Library Lending Division as Supplementary Publication No. SUP 36159 (7 pp.). Copies may be obtained through The Executive Secretary, International Union of Crystallography, 5 Abbey Square, Chester CH1 2HU, England.

$70S$ ribosome preparation was performed (Fig. 2). This sample was precipitated in a test tube with the mixture of organic solvents used for crystallization. Other small-angle patterns were taken from the organic solvent solely to eliminate the contribution of the solvent from the $70S$ ribosome scattering (see dashed line in Fig. 3).

The pinhole small-angle diagrams are limited at $b = 2 \sin \theta/\lambda = 0.02$ nm^{-1} by the primary beam stop.

(a)

55 nm
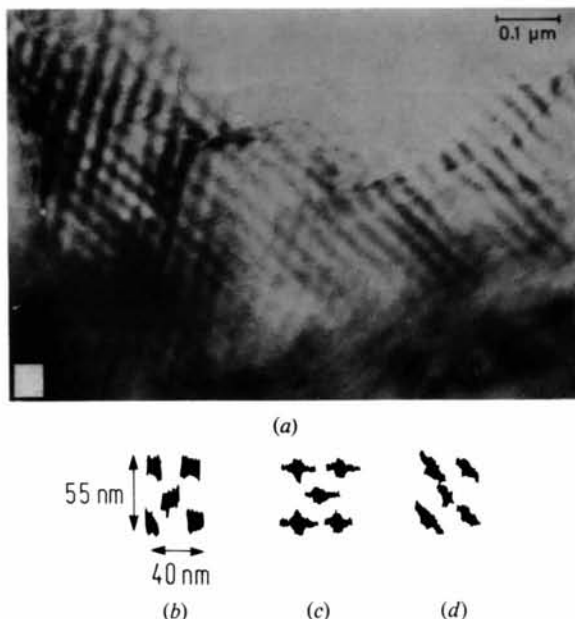
40 nm

(b)   (c)   (d)

Fig. 1. (a) Electron micrograph of a 'crystalline' specimen. The observed macrolattice shows step dislocations and, in the central part, fine horizontal lines orthogonal to the larger lattice edge of 55 nm dividing it into six equidistant parts. (b) Face-centred macrocell and its size. (c) The structure calculated from X-ray small-angle scattering. (d) The same with diagonal stripes. For details see Fig. 15.
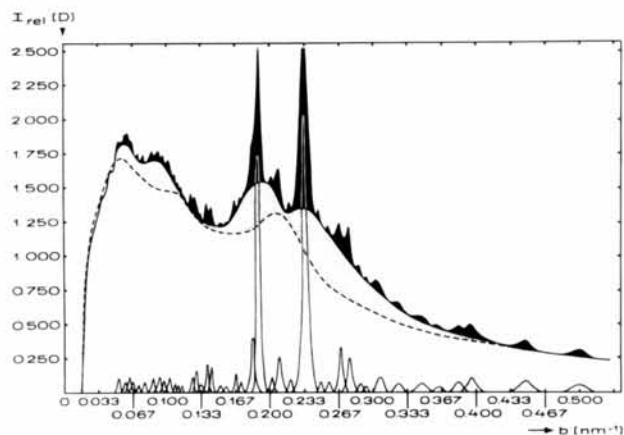
Further investigations were conducted with slit focusing to obtain additional small-angle data. In order to obtain sharp reflections in the small-angle region of $0.02 \lesssim b \leq 0.2$ nm^{-1}, only the vertical flat plate with point or slit focus was used. The film-to-specimen distance was usually 400 mm. After exposure the microcrystalline sample was redissolved and controlled by analytical ultracentrifugation for the $70S$ moving boundary.

III. Indexing of the X-ray diagrams of the super- and sublattice and their paracrystalline distortions

The observed 51 netplane distances d_o and their relative intensities are collected in Table 1. 41 of them can be described by $0kl$ Miller indices and are plotted in the kl diagram of Fig. 4 with orthogonal axes $b = 42 \pm 1$ and $c = 52 \pm 1$ nm (see Kuckuk, 1977; Kuckuk & Paradies 1980). The values d_c calculated herefrom agree, within the error of experiments, with the observed values d_o and the lattice cell dimensions observed in the electron microscope (Fig. 1b). The a axis can be found easily from the strong reflections with $d_o = 18.4$, 15.4 and 13.5 nm and has the same value $a = 42 \pm 1$ nm as the b axis. Each superlattice cell contains therefore $6 \times 8 \times 12 = 576$ subcells. Crystal optics with polarized convergent light confirms that the crystals belong to the hexagonal or tetragonal system (Paradies et al., 1974; Kuckuk, 1977). In Fig. 1 this axis lies obviously orthogonal to the picture plane. We are concerned apparently with a crystal lamella expanded by the b and c axes. From the width of the first 20 reflections with $1/d_o \lesssim 0.133$ nm, one has to learn that the crystal membrane consists of at least 15×15 superlattice cells and has, hence, a lateral size of at least 600 to 800 nm. This again agrees with the electron picture of Fig. 1, where undistorted domains of this size are observable. All these values are collected in Table 2.

Fig. 2. Small-angle X-ray powder pattern of microcrystals of a $70S$ ribosome preparation: ———— the contribution of the precipitate and the solvent; the dotted area corresponds to the amorphous phase.
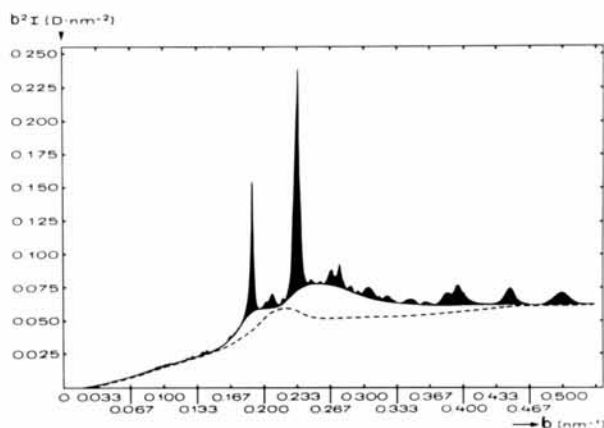

Fig. 3. The $b^2 I(b)$ diagram of Fig. 2. The integral of the dotted area compared with that of the black part leads to 53% amorphous phase in the membrane.

The next interesting fact is that two strong peaks exist in the area of the reflections 080, 081, 082, 084, 090, 091 and 0,0,12, 0,1,12, 0,2,12, 0,3,12. Obviously, the b and c axes consist of 8 and 12 subperiods respectively. The strong reflections with $d_o = 4 \cdot 25$ and

Table 1. *X-ray powder diffraction data of observed* (d_o) *and calculated* (d_c) *netplane distances and their relative intensities* I_{rel}

w very weak reflections measured with special optics, therefore not comparable with other intensities.

h	k	l	d_o(nm)	d_c(nm)	I_{rel}
0	1	1	33·1	32·9	w
0	0	2	26·3	26·0	w
0	2	0	21·4	21·27	16
1	2	0	18·4	19·03	18
0	0	3*	17·2	17·24	15
0	2	2	16·5	16·43	30
1	2	2	15·4	15·33	13
3	0	0	14·5	14·20	12
3	1	0	13·5	13·45	18
3	2	0	11·7	11·80	50
0	3	3	10·8	10·95	31
0	0	5*	10·3	10·34	19
0	4	2	9·7	9·84	29
3	1	4	9·3	9·32	11
0	4	3*	8·9	8·93	10
0	0	6	8·6	8·62	8
0	2	6	7·96	7·99	23
5	0	3	7·63	7·63	38
6	0	0	7·05	7·09	49
6	2	0	6·82	6·84	42
0	0	8	6·39	6·44	18
0	2	8	6·12	6·14	30
7	0	2	5·89	5·92	34
6	0	6	5·47	5·48	136
0	8	0†	5·32	5·32	428
0	8	2†	5·24	5·21	136
0	8	4†	4·92	4·92	35
0	9	1†	4·75	4·75	136
0	8	6	4·53	4·53	35
0	0	12†	4·31	4·31	530
0	2	12†	4·28	4·29	143
6	8	0†	4·25	4·25	188
0	1	13†	4·22	4·22	133
0	3	13†	4·12	4·12	85
6	1	11	3·91	3·92	29
6	0	12	3·72	3·69	126
12	0	0	3·59	3·55	111
7	0	12	3·51	3·52	30
6	2	12	3·45	3·47	16
0	8	12	3·32	3·34	82
6	8	12	3·02	3·00	44
12	0	12	2·75	2·74	82
0	16	0	2·63	2·66	70
6	16	0	2·52	2·51	81
0	16	12	2·25	2·26	82
0	8	24	2·01	2·00	64
12	0	24	1·85	1·84	37
24	8	0	1·69	1·69	28
18	0	24	1·57	1·59	23
0	0	36	1·43	1·44	13
6	16	36	1·22	1·24	8

* Reflections 0*kl* with an odd sum of digits.
† Reciprocal-lattice points within one broad strong peak.

3·02 nm belong to the further ten reflections which cannot be indexed by 0*kl*. If one uses the above mentioned value of $a = 42$ nm, one finds their indices 680 and 6,8,12. Table 1 shows that, by changing some 0*kl* to *h*0*l*, nine reflections with $h = 6$ and four reflections with $h = 12$ can be found (see Fig. 5). In Fig. 6, the remaining 28 reflections with $h = 0$ are plotted. The results are shown in Table 2. The weak reflections 0*kl* for small reciprocal vectors **b** have even sums of digits except three reflections marked with * in Table 1. They indicate a face-centred projection of the macrocell on the *bc* plane. The strong reflections signed with † in Table 1 overlap each other so much in Fig. 3 that they cannot be discriminated from even sums of digits. In Fig. 6, only the reflections with even sums of digits are plotted. The lattice has paracrystalline distortions. The cell edges fluctuate in length statistically by $g_s \simeq 1 \cdot 5\%$, as can be seen from the plot of the integral width δb as a function of $h^2 + k^2 + l^2$ (see Fig. 7). One finds from (20),* at the intersection of the straight curve with the ordinate, a value $1/N \simeq 0 \cdot 0015 \times 42$, hence $N \simeq 15$, which is used for calculating L_a, L_b and L_c in Table 2. From the slope of the line in Fig. 7, one obtains for the relative statistical fluctuation of the macrocell edges b,c (see Appendix II),

$$g_s \simeq 1 \cdot 5\%.$$

As a consequence, the reflections with $b > 0 \cdot 1$ nm^{-1} merge into each other more and more (Appendix I) and the reflections outside the points of the $a_0 b_0 c_0$ lattice disappear in the background.

A remarkable fact is that, around the $a_0 b_0 c_0$ lattice points, some neighbouring reflections of the *abc* lattice are also strong. This is a direct indication that the sublattice also contains paracrystalline distortions. Fig. 8 shows, for example, the small-angle X-ray pattern of a stretched and annealed isotactic polypropylene (PP)
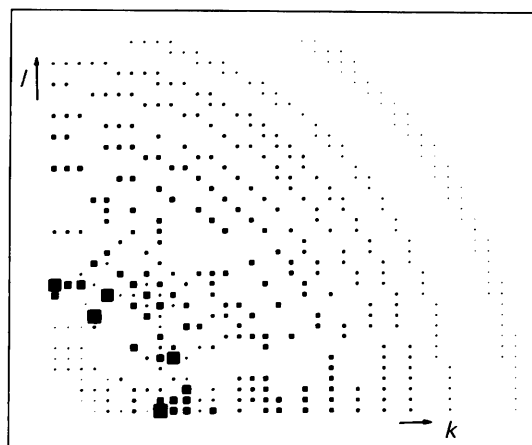
* See Appendix I.

Fig. 4. Positions and intensities of 41 of the observed 51 reflections which can be indexed with 0*kl*. Their intensities are indicated by the sizes of the spots.

Table 2. *The lattice cells a,b,c of the superlattice and a_0,b_0,c_0 of the sublattice with dimensions L_a,L_b,L_c of the superlattice*

g_s, g_{vv} and g_{ww} are respectively the relative lattice distance fluctuations. g_{wv} and g_{vw} are tangential statistical displacements.

Macrocell	$a = (42 \pm 1)$ nm	$b = (42 \pm 1)$ nm	$c = (52 \pm 1)$ nm
	$L_a \gtrsim 600$ nm	$L_b \gtrsim 600$ nm	$L_c \gtrsim 700$ nm
	$g_s \simeq 1 \cdot 5\%$	$g_s \simeq 1 \cdot 5\%$	$g_s \simeq 1 \cdot 5\%$
Subcell	$a_0 = a/6 = 7 \cdot 1$ nm	$b_0 = b/8 = 5 \cdot 3$ nm	$c_0 = c/12 = 4 \cdot 3$ nm
	−	$g_{vv} \simeq 7\%$	$g_{ww} \simeq 7\%$
	−	$g_{vw} \simeq 12\%$	$g_{wv} \simeq 15\%$

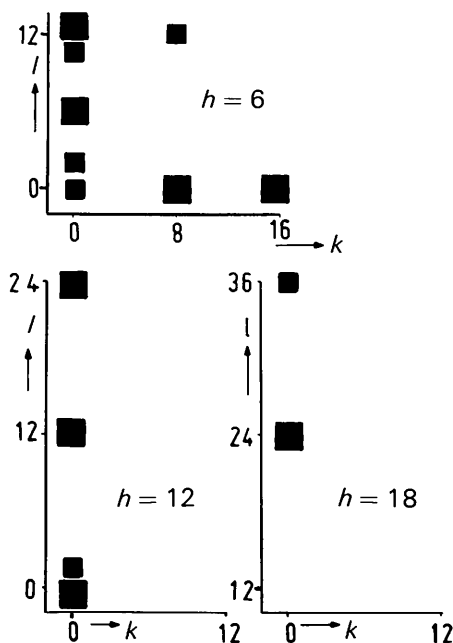
Fig. 5. hkl reflections with $h = 6,12,18$ of the macrolattice with a paracrystalline substructure oriented parallel.
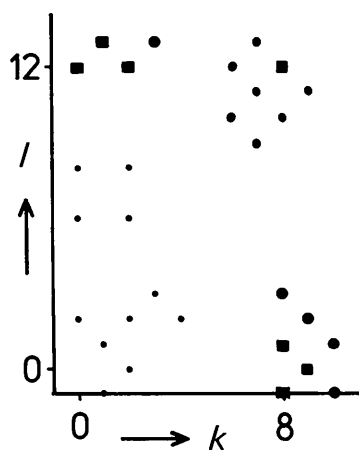
sample (Loboda-Cackovic, Hosemann & Cackovic, 1976). A strong diffuse peak exists in the fibre direction corresponding to a long period of the order of 20 nm which is the distance between the centres of lamella-like assemblies of microparacrystals with g_{ik} values of ~10% (see Appendix I). If many such particle assemblies are arranged three-dimensionally in a well defined superlattice, then the diffuse scattering of one assembly can never be observed and only its intensity at the reciprocal-lattice point of the superlattice (the Bragg window) is visible. The reflection 080 has therefore neighbouring peaks 082, 084, . . .; the reflection 0,0,12 has a neighbour at 0,2,12. This means that the sublattice $a_0b_0c_0$ has lattice axes $b_0 = b/8$ and $c_0 = c/12$, which mostly change their direction in the b_0 and c_0 directions, whereas their lengths fluctuate less. If the index v indicates the direction of $\mathbf{b_0}$ and w that of $\mathbf{c_0}$, then the paracrystalline statistical parameters g_{vw} have values of about

$$g_{vv} \simeq g_{vw} \simeq 0 \cdot 07; \quad g_{vw} \simeq 0 \cdot 12; \quad g_{wv} \simeq 0 \cdot 15 \quad (1)$$

(see Appendix II and Table 2). Fig. 9 shows an example of paracrystalline distortions of the type in (1), the only difference is that $g_{vv} \simeq g_{ww} \simeq 0$ and $g_{vw} \simeq g_{wv} \simeq 0 \cdot 28$.

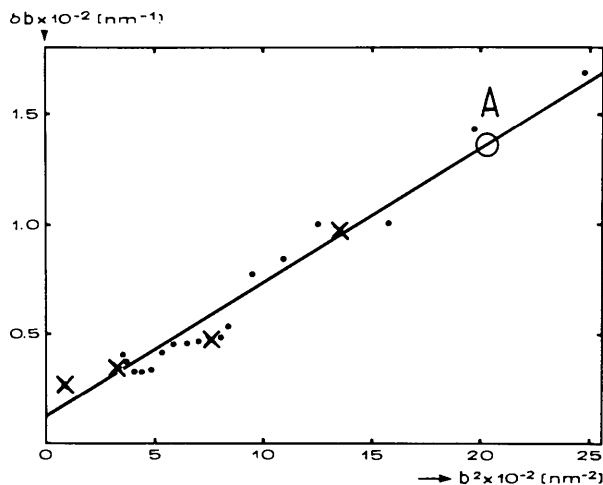Fig. 6. The same as in Fig. 5 for 0kl. ■ Strong, ● medium, • weak.

Fig. 7. The integral widths δb of the reflections $hk0$ as a function of $b^2 = (2 \sin \theta/\lambda)^2$ reveal isotropic paracrystalline distortions of the macrolattice of $g_s \simeq 1 \cdot 5\%$ and lattice sizes of more than 600 nm.
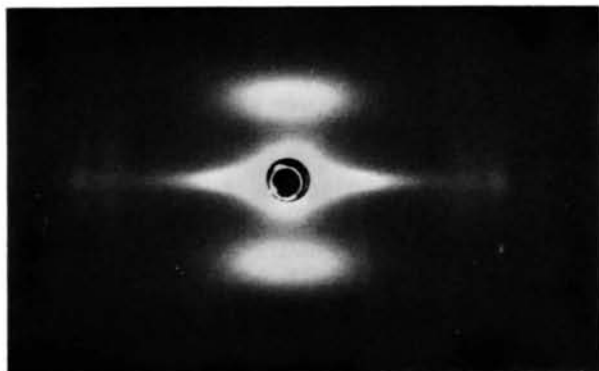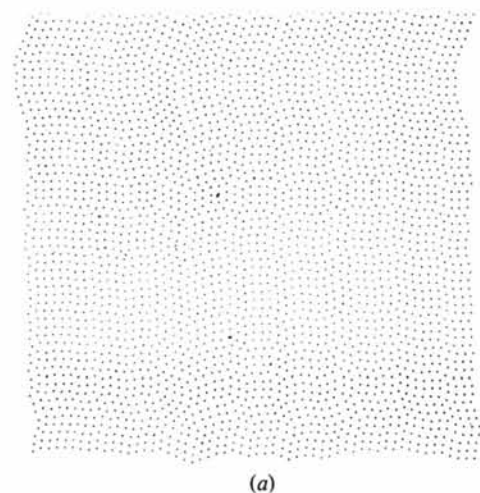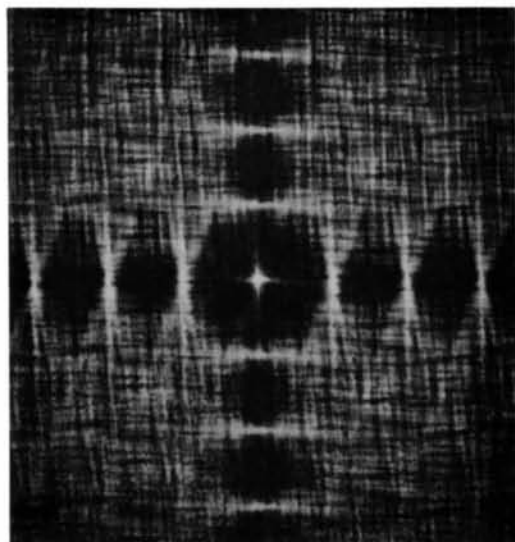
Fig. 8. Small-angle X-ray diagram of synthetic cold-stretched linear isotactic polypropylene. The fibre axis is in the vertical direction.

(a)

(b)

Fig. 9. A two-dimensional paracrystal with distortions $g_{12} = g_{21} \simeq 28\%$ and $g_{11} = g_{22} \simeq 0\%$. (a) Two-dimensional point lattice model, (b) its Fraunhofer pattern.

The higher orders of 010 and 001 are therefore better developed and 011 is much diffuser than in Fig. 6. It is essential that with this type of paracrystalline distortions the reflections 010 and 001 are much broadened in tangential directions. The motifs within the $\mathbf{b}_0 \mathbf{c}_0$ lattice cells have therefore relatively well defined distances, but with varying directions. In synthetic polymers, on the other hand, the motifs are micro-paracrystals 10 to 30 nm in all three dimensions and densely packed together to form lamellae, which have g_{uu} values of the order of 10%. This gives rise to the diffractions shown in Fig. 8 where two meridional reflections are produced by a period of 20 to 40 nm, orthogonal to the lamellae surfaces.

The next important question is: What is the content of a ribosome subcell? A first answer is that about 47% of the volume of a macrocell is 'crystalline' and 53% is 'amorphous'. This can be calculated from the powder pattern of Fig. 2 in the $b^2 I(b)$ plot of Fig. 3. The white field under the dashed curve gives the scattering of the solvent adapted in height to the intensity curves of Figs. 2 and 3. The grey area between the white and black areas yields, after integration in the $b^2 I$ plot, 53%. This means that, similar to synthetic polymers, the crystalline phase is imbedded in the amorphous phase.

In the next section, it is shown that 47% of the subcells contain cylindrically shaped particles aligned parallel to the a axis. They form some well constructed compounds, within an **abc** lattice cell, which build up a superlattice as can be seen in Fig. 1. To understand the diffraction pattern, it is not necessary to know the ideas of shells. The mean electron density distribution of an **abc** lattice cell therefore can be recognized only through the Bragg windows at the positions of the reflections of the superlattice. The fluctuation between nth neighbours of these compounds increases with $\sqrt{n}$ and the relative fluctuation of a sequence of n vectors $\mathbf{c}_0$ or $\mathbf{b}_0$ is therefore given by $g_{vw}/\sqrt{n}$ or $g_{vv}/\sqrt{n}$. This is the reason for the small value $g_s \simeq 1.5\%$ in a superlattice. In synthetic polymers, on the other hand, the lamellae are not so well organized and build up bundles with tremendously fluctuating a, b, c axes. The Bragg windows now are not of the crystalline-like type, they are amorphous-like, and one therefore can observe directly the mean diffraction pattern of an $\mathbf{a}_0 \mathbf{b}_0 \mathbf{c}_0$ cell without being restricted by Bragg windows (Fig. 8). Nevertheless, ribosomes and synthetic polymers have one feature in common: chain molecules in ribosomes are arranged parallel to the a axis, in synthetic polymers they are orthogonal to the lamellae.

IV. Analysis of the paracrystalline Q function

The inverse transformation of the observed intensity function $I(\mathbf{b})$ is a three-dimensional function of the vector $\mathbf{x}$ in physical space; this does not reveal the

structure $\rho(\mathbf{x})$ of the electron distribution but its convolution square (symbol $\tilde{2}$; see for detail Appendix III):

$$\mathscr{F}^{-1}\, I(\mathbf{b}) = Q(\mathbf{x}) = \overset{2}{\tilde{\rho}}(\mathbf{x}) = \int \rho(\mathbf{y})\, \rho(\mathbf{y} + \mathbf{x})\, \mathrm{d}y^3;$$

$$b = 2\sin\theta/\lambda. \tag{2}$$

In our case, $I(\mathbf{b})$ is given by the integral intensities I_{hkl} of the reflections of the macrolattice. Now we introduce the normalized components u, v, w of the space vector $\mathbf{x}$, which are integers at the edges of the macrocells. We obtain from (2),

$$Q(u, v, w) = \sum_{k,k,l} I(h, k, l) \exp\left[2\pi i(hu + kv + lw)\right]. \tag{3}$$

$Q(0, v, w)$, calculated from the relative intensity data of Table 1, is plotted in a perspective way in Fig. 10. In Fig. 11, the Fourier transform $\bar{Q}(v,w)$ of $I(0,k,l)$ is drawn. According to Appendix IV, it is just the two-dimensional convolution square of the projection of the electron density distribution on the vw plane. Each subcell $(\mathbf{b_0 c_0})$ of the Q function contains a cylindrical density cloud whose axis is oriented parallel to the 7 nm long a_0 axis. The diameter of the cylinder depends, in contrast with the Patterson (1934) function, not only on the diameter of molecular strings, but also on their paracrystalline distortions (equation 1). The larger g_{wv} value, for instance, points out that the cell edges $\mathbf{b_0}$ have strongly varying directions. This gives rise to the density bands in Fig. 11 which connect neighbouring cylinders in the v direction. The cylinders with diameter $D \simeq 2 \cdot 9$ nm are therefore composed of the real diameter D_0 of cylindrical molecules and their statistical paracrystalline displacement. The product of $g_{wv} \times a_v = 0 \cdot 12 \times 5 \cdot 3 = 0 \cdot 64$ nm is, for instance, according to (1) and (18), the fluctuation of the cylinders in the v direction. The diameter D_0 of the convolution square of the cylindrical molecules is therefore given by

$$D_0 = (D^2 - 0 \cdot 64^2)^{1/2} \simeq 2 \cdot 8 \text{ nm} \tag{4}$$

(see Appendix V). The diameters of the cylinders themselves are therefore given by

$$D_0/\sqrt{2} \simeq 2 \cdot 0 \text{ nm} \tag{5}$$

because they are the convolution root of the cylinders of the Q function. These cylinders contain obviously the above mentioned 47% electrons of the crystalline phase. Although the Q function of Fig. 10 shows a nearly uniform distribution of the cylinders in the macrocell, its convolution root $\bar{\rho}$ will nevertheless show a distinct distribution in the macrocell. The cylinders build up two clusters within one macrocell as will be shown below.

V. Distribution of cylinders in a macrocell

As mentioned above, the cylinders of the density $\rho(\mathbf{x})$ are not distributed uniformly in a macrocell, because the weights of the cylinders of the $\bar{Q}$ function (Fig. 11) vary slightly. As shown below, they build up two clusters. With regard to the lack of quantitative intensity data, we will restrict our discussion to the analysis of the reflections $0k0$.

From (3) and Appendix IV, one learns that

$$\sum_k I(0k0) \exp\left(2\pi i k v\right) = \bar{Q}(v) = \int\int Q(u,v,w)\, \mathrm{d}u\, \mathrm{d}w. \tag{6}$$

Strictly speaking, one has to integrate solely over even k values, because the lattice cell is face-centred. For convenience we integrate over all integer k values,
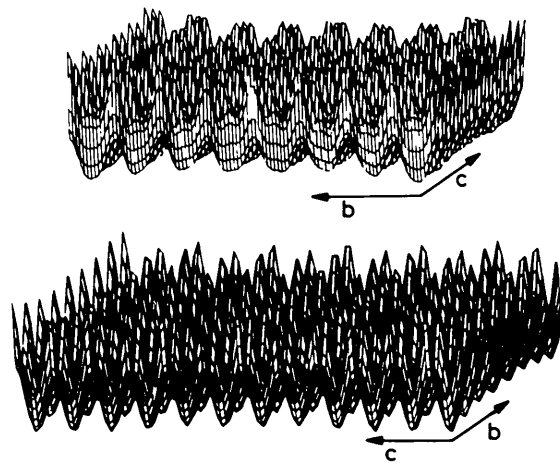

Fig. 10. The function $Q(0,v,w)$ calculated by Fourier transformation of $I(hkl)$ plotted perspectively orthogonal. b and c are the axes of the macrocell.
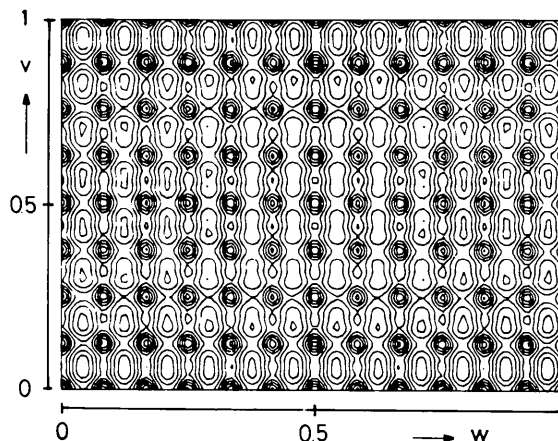

Fig. 11. Function $\bar{Q}(v,w)$ as counter diagram. The two-stranded helices orthogonal to the bc plane are visible.

because only the strong reflections near $k = 8$ are important and are not even resolved in single reciprocal-lattice points on account of the paracrystalline g_s value which allows them to merge into each other as explained above. The advantage of this procedure is that we have to reconvolute now only a primitive superlattice cell. Equation (6) is, according to Appendix IV, nothing but the one-dimensional convolution square of the two-dimensional projection $\bar{p}$ of p of this primitive cell along the b axis. $\bar{Q}(v)$ is plotted in Fig. 12 which shows, according to Fig. 11, eight peaks within one macrolattice cell, all having nearly the same shape. Now we are engaged in a one-dimensional problem: the deciphering of the two-dimensional projection of Q on the v axis. If $\bar{p}_0$ is the two-dimensional projection of the electron density of one macrocell, then the density projection $\bar{p}$ of the whole crystal is given by

$$\bar{p}(v) = \sum_n \bar{p}_0(v - n); \quad n \text{ integer.} \quad (7)$$

In each macrocell, $n = 0, 1, 2, \ldots, \bar{1}, \bar{2}, \ldots,$ with $b = 42$ nm, the same density projection $\bar{p}_0$ exists. It has values different from zero for $v = 0$ to $1, v = 1$ to $2, v = 2$ to 3 and so on. The $\bar{Q}(v)$ function, as its convolution square [see (2)], is given by

$$\bar{\bar{Q}}(v) = \sum_n \bar{\bar{Q}}_0(v - n); \quad \bar{\bar{Q}}_0 = \bar{\bar{p}}_0^2. \quad (8)$$

Unfortunately, $\bar{\bar{Q}}_0$, the convolution square of $\bar{p}_0$, extends over two macrocells from $v = -1$ to $+1$ or from $v = 0$ to $+2$ and so on. Therefore, we have two overlapping $\bar{\bar{Q}}_0$ functions in the lattice cell $0 \le |v| \le 1$ of Fig. 12, the right part of $\bar{\bar{Q}}_0(v)$ and the left part of $\bar{\bar{Q}}_0(v - 1)$.

VI. Convolution root of the $\bar{\bar{Q}}_0$ function

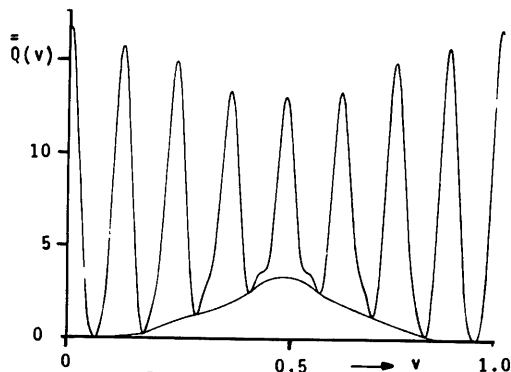We have discussed above the fact that each macrocell produces obviously continuous more or less diffuse

scattering similar to the small-angle scattering of polypropylene (PP) (Fig. 8). Many such macrocells build up the ribosome paracrystal and, as a consequence, the continuous scattering function $\bar{Q}_0$ of one macrocell is only observable at the points of reciprocal superlattices $(\mathbf{a^*},\mathbf{b^*},\mathbf{c^*})$. Therefore, one can obtain the scattering function of one macrocell by interpolation between the observable intensity peaks hkl. Ambiguity does not exist, because $\bar{Q}_0$ has no zero values. To calculate the convolution root, it is sufficient to introduce values also at the lattice points $k \pm \frac{1}{2}$. The function $\bar{Q}_2(v)$ was calculated in this way (Fig. 13):

$$\bar{Q}_2(v) = \sum_k I(0,k/2,0) \exp(\pi i k v), \quad k \text{ integer.} \quad (9)$$

The reciprocal-lattice points have now only half of their former distances. $\bar{Q}_2(v)$ is therefore given by

$$\bar{\bar{Q}}_2(v) = \sum_n \bar{\bar{Q}}_0(v + 2n). \quad (10)$$

Since the distance of the $\bar{Q}_0$ function is now $2n$, no overlapping of adjacent $\bar{Q}_0$ functions can take place. The background in Figs. 12 and 13 is an artefact, because, by calculating $\bar{Q}(v)$ with (6), the value $I(010)$ was omitted arbitrarily because $I(000)$ is not observable and hence $I(010)$ cannot be obtained as an average of the neighbouring I values. The result is a diffuse background in Q,

$$_u\bar{\bar{Q}} \simeq -A \cos 2\pi v,$$

which can be removed by introducing $I(010) = A$. As a consequence, the diffuse background $_u\bar{\bar{Q}}_2$ in Fig. 13 has also no physical meaning. It explains easily the background $_u\bar{\bar{Q}}$ of Fig. 12 because, according to (8),

$$_u\bar{\bar{Q}}(0) = _u\bar{\bar{Q}}(n) = _u\bar{\bar{Q}}_0(0) + _u\bar{\bar{Q}}_0(1) = 0 + 6 \cdot 5$$

$$_u\bar{\bar{Q}}(\tfrac{1}{2}) = 2_u\bar{\bar{Q}}_0(\tfrac{1}{2}) = 10;$$

hence

$$_u\bar{\bar{Q}}(\tfrac{1}{2}) - _u\bar{\bar{Q}}(0) = 3 \cdot 5.$$

This is just the difference between the largest and smallest values of $_u\bar{\bar{Q}}$ drawn in Fig. 12.

Fig. 12. Function $\bar{\bar{Q}}(v)$ calculated by Fourier transformation $I(0k0)$. The background is practically given by $-A \cos 2\pi v$ and disappears if the reflection $I(010) = A$ is introduced into equation (6).
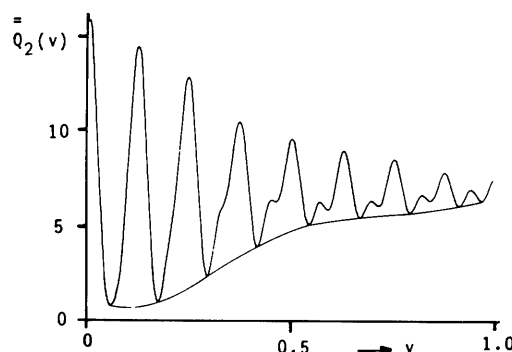

Fig. 13. Function $\bar{\bar{Q}}_2(v)$ calculated by Fourier transformation of $I(0,k/2,0)$. The diffuse background has no physical meaning (see Fig. 12).

The values A_q of the maxima of the eight distinguished peaks of $\bar{Q}(v)$ and the values A_{0q} of $\bar{Q}_2(v)$ are collected in Table 3. The error of the A_{0q} values at the boundaries of $\bar{Q}_2(v)$ is relatively large. This uncertainty can be cancelled, more or less, because, from the above discussed overlapping effect, one obtains the relation

$$A_{0,q} + A_{0,8-q} = A_q. \tag{11}$$

Such calculated A_{0q} values are collected in the third line of Table 3 and plotted in Fig. 14. $\bar{p}(v)$ itself has seven distinct values B_q, which are also collected in Table 3. From (2), follows

$$A_{0\bar{n}} = A_{0n} = \sum_{q=0}^{7} B_{q+n} B_q. \tag{12}$$

We will deduce now a recursion formula and assume that the A_{0n} values have an error a_n, B_q an error b_q, whilst A_{0n} and B_q are the real parameters of the structure. Then, one obtains, instead of (12),

$$A_{0n} + a_n = \sum_{q=0}^{7} (B_{q+n} + b_{q+n})(B_q + b_q). \tag{13}$$

Removing herefrom the terms of (12), one obtains, neglecting b_q^2,

$$a_n = \sum_{q=0}^{7} (B_{q+n} b_q + B_q b_{q+n}). \tag{14}$$

This can be transformed into a matrix equation

$$a_n = (T_{qn}) b_q \quad \text{with} \quad (T_{qn}) = (B_{q+n} + B_{q-n})$$
$$0 \le (q+n) < 7; \quad 0 < (q-n) < 7. \tag{15}$$

Herefrom one obtains directly the error values b_q of B_q as a function of the error values a_n,

$$b_q = \frac{(T_{rn})}{T_{qn}}. \tag{16}$$

The difference between solutions I, II and III is that the tentative first solution I is symmetrical with respect to $q = 3 \cdot 5$, while the iterated solutions II and III both have a kind of symmetry centre at $q = 3$. This shift of q is without any significance as long as the boundaries of the macrocell do not interfere. The position of a macrocell then is absolutely arbitrary and the same is true for the subcells. T_{rn} is the reciprocal matrix which is identical with all terms of T_{qn} except those in the column $r = q$. Here the T_{qn} terms are replaced by a_q values.*

A first approvable solution I is given in Table 3 with its differences a_q between calculated and measured weights A_{0q}. Most of them are of the order of a few percent. The value of a_6 is extremely large ($\sim 50\%$). These errors are introduced into (16). By computer, one obtains the correction terms b_k for the first solution. The corrected B_q values yield new A_{0n} values from (12)

* A similar procedure for calculation of the convolution square root was published by Bradaczek & Luger (1978).
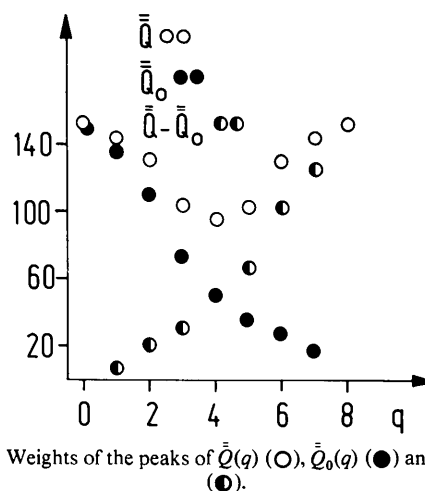

Fig. 14. Weights of the peaks of $\bar{Q}(q)$ (O), $\bar{Q}_0(q)$ (●) and $\bar{Q}_0(8-q)$ (◑).

Table 3. *The terms A_q of $\bar{Q}$, A_{0q} of $\bar{Q}_0$ and three different solutions* I, II, III *for the convolution root B_q and the failures a_q of A_q*

N_q number of subcells within the cross sections q of a tetramer orthogonal to the b axis.

Solution number	$q = 8v$	0	1	2	3	4	5	6	7	8
	A_q	152	143	130	103	95	103	130	142	152
	A_{0q}	152	136	110	73	47	30	20	7	0
I	$B_q/\sqrt{5}$	1	1	2	3	3	2	1	1	
	a_q	2	1	0	−7	−1	5	10	2	
II	$B_q/\sqrt{5}$	0·7	2·2	2·6	3·1	2·4	1·7	0·5	1·1	
	a_q	−4	0·5	2·5	−1	−0·5	0·5	0·15	0·01	
III	$B_q/\sqrt{5}$	1·1	1·2	2·9	2·7	2·9	1·7	1·1	0·5	
	a_q	−4	0·6	2·5	−1	−0·5	0·5	0·16	0·01	
$\frac{1}{2}$(II + III)	$B_q/\sqrt{5}$	0·9	1·7	2·7	2·9	2·7	1·7	0·8	0·8	
IV	N_q	2	9	15	25	30	25	15	9	2

with new a_q errors. The process is iterated until the mean square deviation

$$\frac{1}{N(N-1)} \sum_n^N a_n^2$$

reaches a minimum. In most cases this happens after less than 100 iteration steps. This solution II is also tabulated in Table 3. A new iteration process was started and led to solution III. Within the error of the experiment, it is equivalent to solution II.

It is interesting to note that structures without a centre of symmetry can be analysed in the same way as those which have a symmetry centre. Two cases have to be differentiated:

(1) The A_{0q} are the exact values of a convolution product. The matrix $|T_{rn}|$ becomes singular if the exact solution is found. The mean square deviation then converges to zero and the process is terminated. On account of the inaccuracy of intensity measurements this case is an academic one.

(2) If the A_{0q} values have errors, only an approximate solution can be found. The minimal mean square deviation depends on these errors. If we continue the iteration process, it increases again. Another minimum with different solution may be obtained later on. Moreover, the solution also depends somewhat on the initial B_q values. In order to obtain all possible solutions, a Monte-Carlo procedure was applied to choose the starting values of B_q. It is interesting to note that in the present example only two slightly different solutions II and III were found with very small deviations a_q from the X-ray data of A_{0q} (Table 3). Now we have to take into account the fact that the projection of the macrocell on the vw plane is face centred as proved by the electron micrograph (Fig. 1a) and the X-ray $0kl$ reflection at small b values, whose sum of digits is even (Table 1) except for three reflections (*).

The respective body-centred $\bar{Q}$ function shows, in contrast to Figs. 11 and 12, higher peaks not only at the edges but also in the centre, $v, w = \frac{1}{2}, \frac{1}{2}$. The function is still quite inappropriate for calculating the convolution root because one more overlapping Q_0 function occurs than in Fig. 12. Therefore we neglected its calculation.

VII. Discussion of the structure

Small-angle X-ray diffraction proves that, by artificial crystallization, ribosomes can build up microcrystallites bigger than 600×600 nm with face-centred tetragonal macrocells of 42×52 nm. This is in good agreement with electron micrographs. Orthogonal to the surface of the bc plane there appear parallel aligned cylinders, about 2·0 nm in diameter, with fibrillar paracrystalline distortions. Within one macrocell, $6 \times 8 \times 12 = 576$

subcells exist. About 47% of them belong to the face-centred positioned compounds. Therefore, each of them consists of

$$\frac{1}{2} \times 0\cdot47 \times 576 \simeq 136 \text{ subcells.} \qquad (17)$$

The height of the macrocell in the fibre direction is 42 nm. Therefore, each cylinder is $\frac{1}{6}$ of this in length $= 7\cdot2$ nm and about 2·0 nm in diameter. This agrees well with the size of the two-stranded fragments of rRNA obtained by digestion with enzymes which only affect the single-chain regions of the RNA (Timasheff et al., 1961; Cox & Kanagalingam, 1967; Spencer et al., 1969). From all these facts, and considering the literature reviewed in the Introduction, we conclude that the cylinders are the two-stranded helices first detected by Schlessinger (1960), and amply confirmed by many subsequent works. The two components consisting of 136 subcells each are tetramers of $70S$ ribosomes each containing $136:4 = 34$ cylinders.

A method, first published by Hosemann & Bagchi (1962), is applied to calculate the convolution root of the projection of the Q function on the b axis. The first direct information on the three-dimensional structure of a tetramer of $70S$ ribosomes can be obtained in this way. If we take the averaged B_q values of Table 3,II and 3,III, we obtain, after multiplying them by ~10, integers N_q (see Table 3,IV) which show the total sum of ~136. They define the number of subcells within each cross section of one tetramer orthogonal to the b axis.

A comparison of the experimental density of the crystal, obtained by the flotation method, with theoretical density calculations leads to the same conclusion that about eight ribosomes are placed within one macrocell and that about half of the macrocell volume is filled with organic solvent.

Fig. 15 shows a schematic picture of all essentials of this paper. Each cylinder represents a subcell of the crystalline-like phase. Two tetramers are in one macrocell. The first has its centre at $(q,r) = (3,4)$, the other at $(7,10)$ (only one half of the second tetramer is drawn). The number N_q of subcells within one tetramer is represented by the number of cylinders. The open question, how the cylinders are distributed within each cross section q, remains. But one thing is evident: the tetramers have shapes with thin tails in both directions parallel to the b axis as drawn in Fig. 1(c). If they are deformed (Fig. 1d), the diagonal stripes of Fig. 1(a) are understandable. The model of Tischendorf et al. (1975) also shows such kinds of tails. The columns of cylinders are statistically shifted (see Fig. 9), mathematically expressed by the large g_{vw} and g_{wv} values of (1). The inner structure of the two-stranded helices depends on the wide-angle reflections which are not yet taken into account by our analysis. Their paracrystalline flexibility nevertheless allows them to build up a reliable undistorted macrolattice as explained above. The

ribosomal proteins different in size, shape and primary sequence generate obviously the large liquid-like distortions within the macrolattice cells similar to the paracrystalline structure of synthetic polymers.

The shape of the tetramers can be described now not only by the radius of gyration, but also by three different orthogonal axes. As shown in Appendix VI, the average size of a tetramer of 70S ribosomes in the directions of the axes a,b,c of the macrolattice can be calculated as $34 \times 29 \times 17$ nm $\simeq 16\ 700$ nm^3, whilst the accurate value for the volume of one tetramer is given by (17) and Table 2 as $136 \times 7{\cdot}1 \times 5{\cdot}3 \times 4{\cdot}3 \simeq 22\ 000$ nm^3. In agreement, Hill *et al.* (1969) found for the volume of one 70S ribosome about a quarter of this value: $18 \times 20 \times 16 = 5760$ nm^3.

In Fig. 1(a) one can observe a domain of about ten macrocells with a fine striation containing six parallel streaks within a macrocell orthogonal to the c axis. This can be easily explained by the model of Fig. 15. In the cross sections $q = 3$ and 7, three cylinders are plotted with lengths $6 \times 7{\cdot}1$ nm alternating with three cylinders $4 \times 7{\cdot}1$ nm long, the former at odd and the latter at even values of $12w$. They produce the six streaks per lattice cell orthogonal to the c axis. The small domain of striation can be explained by the fact that the subcells have large paracrystalline fibre-like distortions defined by (18). It is no wonder that the orientation of these
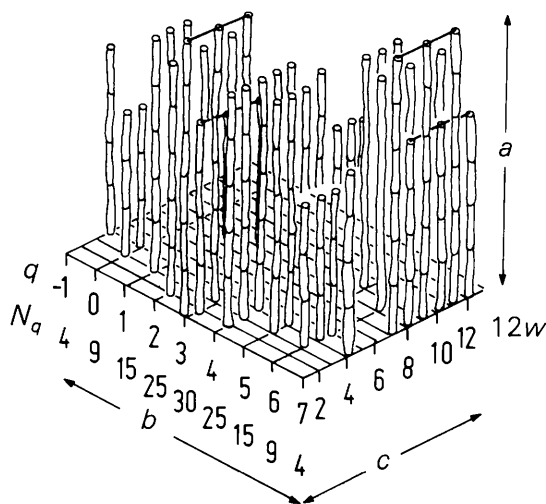
domains is not everywhere in a position to be detected in the electron microscope. There are of course many other possible structures. Our model is just one of these possibilities. Nevertheless, the quantitative parameters given in Tables 1–3 are reliable and define to a high degree most of the solutions.

The crystalline arrangement of the different two-stranded helices (Fig. 15) of ribosomal RNA parallel to the a axis within the ribosome provides an explanation for some well known characteristics of ribosomes: (1) the highly organized and compact configuration; (2) the reconstruction of ribosomes from their basic components (Nomura, 1973); and (3) the large exothermic enthalpy change during refolding (Wong, Dünn & Binford, 1974). It is interesting to note that basic theoretical considerations of the evolution of biological macromolecules, especially RNA, lead to a hairpin-like model of parallel aligned double-stranded RNA (Kuhn, 1980) like the one of rRNA described in our paper.

Microcrystals of 80S ribosomes can be obtained within the cell by hypothermia (Byers, 1967; Unwin & Taddai, 1977). This seems to be quite a common feature in nature during hibernation. This procedure ensures an enormous reduction of the energy turnover per cell because of reduction of the protein synthesis to a very low level. In addition, Yonath (1980) showed that crystallized 50S subunits of bacillus ribosomes are biologically fully active after a long period of crystalline storage.

Improved techniques are necessary to demonstrate the presence of tetramers of 70S ribosomes in electron micrographs of single crystals and to obtain more stable and larger crystals for X-ray diffraction. The measurement of the intensity $I(000)$ would make it possible, in addition, to calculate the absolute electron density distribution.

Fig. 15. A model of the structure of the ribosome membrane. The cylinders represent the two-stranded helices and are arranged orthogonal to the bc membrane plane. They build up two tetramers each containing 136 subcells which are in face-centred positions. Their number per section q within one tetramer is given by N_q, their distribution within each area is arbitrarily chosen, but performed in such a way that the shape of the tetramer is similar to that in Fig. 1(c). The centres of the tetramers lie at $q,12w = 3,4$ and 7,10 and $\bar{1},10$. The tetramer $\bar{1},10$ and the outer part of the tetramer 7,10 are not plotted for convenience. The neighbouring cylinders on lines $3,12w$ and $7,12w$ have alternating lengths $6a_0$ and $4a_0$ which produce the fine striation orthogonal to the c axes in the centre of Fig. 1(a). The staggered contours of the fibrils symbolize their paracrystalline distortions.

References

BRADACZEK, H. & LUGER, F. (1978). *Acta Cryst.* A**34**, 681–683.

BROWN, G. L. & ZUBAY, G. (1960). *J. Mol. Biol.* **2**, 287–296.

BRUSKOV, V. I. & KISELEV, N. A. (1968). *J. Mol. Biol.* **37**, 367–377.

BUSH, C. A. & SCHERAGA, H. A. (1967). *Biochemistry*, **6**, 3036.

BYERS, B. (1967). *J. Mol. Biol.* **26**, 155–167.

CONNORS, P. G. & BEEMAN, W. W. (1972). *J. Mol. Biol.* **71**, 31–37.

COX, R. A. (1969). *Biochem. J.* **114**, 743–751, 753–767, 769–774.

COX, R. A. & KANAGALINGAM, O. F. (1967). *Biochem. J.* **103**, 431–452.

DEUSSER, E. (1972). *Mol. Gen. Genet.* **119**, 249–256.

DIBBLE, W. E. (1964). *J. Ultrastruct. Res.* **11**, 363–373.

DREISSIG, W., HOSEMANN, R. & NEMETSCHEK, T. (1974). *Z. Naturforsch. Teil C*, **29**, 516–520.

FOLKHARD, W., PILZ, I., KRATKY, O., GARRETT, R. & STÖFFLER, G. (1975). *Eur. J. Biochem.* **59**, 63–71.

FULLER, W. (1961). *J. Mol. Biol.* **3**, 175–184.

GAFFNEY, P. T. & CRAVEN, G. (1978). *Proc. Natl Acad. Sci. USA*, **75**, 3128–3132.

HALL, C. E. & SLAYTER, H. S. (1959). *J. Mol. Biol.* **1**, 329–332.

HART, R. G. (1962). *Biochim. Biophys. Acta*, **60**, 629–637.

HART, R. G. (1965). *Proc. Natl Acad. Sci. USA*, **53**, 1415–1420.

HILL, W. E. & FESSENDEN, R. J. (1974). *J. Mol. Biol.* **90**, 719–726.

HILL, W. E., THOMPSON, J. D. & ANDEREGG, J. W. (1969). *J. Mol. Biol.* **44**, 89–102.

HOSEMANN, R. & BAGCHI, S. N. (1962). *Direct Analysis of Diffraction by Matter.* Amsterdam: North-Holland.

HOSEMANN, R., BONART, R. & NEMETSCHEK, T. (1974). *Colloid Polym. Sci.* **252**, 912–919.

HOSEMANN, R., DREISSIG, W. & NEMETSCHEK, T. (1974). *J. Mol. Biol.* **83**, 275–280.

HOSEMANN, R. & NEMETSCHEK, T. (1973). *Kolloid Z. Z. Polym.* **251**, 53–60.

HOSEMANN, R., WEICK, D., VOGEL, W. & MÜLLER, N. (1974). *Ber. Bunsenges. Phys. Chem.* **78**, 1358–1366.

HUXLEY, H. E. & ZUBAY, G. (1960). *J. Mol. Biol.* **2**, 10–18.

KLUG, A., HOLMES, K. C. & FINCH, J. T. (1961). *J. Mol. Biol.* **3**, 87–100.

KUCKUK, E. D. (1977). Nat. Dissertation, Freie Universität Berlin.

KUCKUK, E. D. & PARADIES, H. H. (1980). Submitted to *Biochim. Biophys. Acta.*

KUHN, H. (1980). *Abh. Braunschw. Wiss. Ges.* **31**, 105–127.

LANGRIDGE, R. (1969). *Science*, **140**, 1000.

LANGRIDGE, R. & HOLMES, K. C. (1962). *J. Mol. Biol.* **5**, 611–617.

LAUFFER, M. A. & BENDET, J. J. (1954). *Adv. Virus Res.* **2**, 241–256.

LOBODA-CACKOVIC, J., HOSEMANN, R. & CACKOVIC, H. (1976). *Polymer*, **17**, 303–308.

LUBIN, M. (1968). *Proc. Natl Acad. Sci. USA*, **61**, 1454–1461.

MOORE, P. B., ENGELMANN, D. M. & SCHOENBORN, B. P. (1974). *Proc. Natl Acad. Sci. USA*, **71**, 172–176.

MOORE, P. B., ENGELMANN, D. M. & SCHOENBORN, B. P. (1975). *J. Mol. Biol.* **91**, 101–120.

NANNINGA, N. (1967). *J. Cell. Biol.* **33**, C1–C6.

NANNINGA, N. (1968). *Proc. Natl Acad. Sci. USA*, **61**, 614–620.

NEMETSCHEK, T. & HOSEMANN, R. (1973a). *Kolloid Z. Z. Polym.* **251**, 1044–1056.

NEMETSCHEK, T. & HOSEMANN, R. (1973b). *Naturwissenschaften*, **6**, 304–305.

NEWESELY, H., HOSEMANN, R. & UTHER, B. (1980). *Z. Naturforsch. Teil C*, **35**, 177–187.

NOMURA, H. (1973). *Science*, **179**, 864–873.

NONOMURA, Y., BLOBEL, G. B. & SABATINI, D. (1971). *J. Mol. Biol.* **60**, 303–323.

PARADIES, H. H., KUCKUK, E. D., KLOTZ, G., ZERBAN, H. & DEUSSER, E. (1974). *Hoppe-Seyler's Z. Physiol. Chem.* **355**, 1557–1561.

PARFAIT, R. P., KOCH, M. H. J., CRICHTON, R. R., HAAS, J. & STUHRMANN, H. B. (1978). International Biophysics Congress, Kyoto, Japan, September 1978.

PATTERSON, A. L. (1934). *Phys. Rev.* **46**, 372–375.

RICH, A. & WATSON, J. D. (1954). *Nature (London)*, **173**, 995–996.

SCHLESSINGER, D. (1960). *J. Mol. Biol.* **2**, 92–95.

SPENCER, M., PIGRAM, W. J. & LITTLECHILD, J. (1969). *Biochim. Biophys. Acta*, **179**, 348–359.

SPIRIN, A. S., KISELEV, N. A., SHAKULOV, R. S. & BOGDANOV, A. A. (1963). *Biokhimiya*, **28**, 920–930.

TIMASHEFF, S. N., WITZ, J. W. & LUZZATI, U. (1961). *Biophys. J.* **1**, 525–537.

TISCHENDORF, G. W., ZEICHARDT, H. & STÖFFLER, G. (1975). *Proc. Natl Acad. Sci. USA*, **72**, 4820–4824.

UNWIN, P. N. T. & TADDAI, C. (1977). *J. Mol. Biol.* **114**, 491–506.

VENABLE, J. H., SPENCER, M. & WARD, E. (1970). *Biochim. Biophys. Acta*, **209**, 493–500.

WEBER, H. J. (1972). *Mol. Gen. Genet.* **119**, 233–248.

WHEELER, E. J. & LEWIS, D. (1977). *Calcified Tissue Res.* **24**, 243–248.

WILKINS, H. F., ZUBAY, G. & WILSON, H. R. (1959). *J. Mol. Biol.* **1**, 179–185.

WONG, K.-P., DÜNN, J. M. & BINFORD, J. S. (1974). *FEBS Lett.* **41**, 211–217.

YONATH, A. (1980). *Biochem. Internatl.* In the press.

ZUBAY, G. & WILKINS, M. H. F. (1960). *J. Mol. Biol.* **2**, 105–112.